

# Direct Probe of Topological Order for Cold Atoms

Dong-Ling Deng, Sheng-Tao Wang, and L.-M. Duan

*Department of Physics, University of Michigan, Ann Arbor, Michigan 48109, USA and  
Center for Quantum Information, IIIS, Tsinghua University, Beijing 100084, PR China\**

(Dated: November 18, 2014)

Cold-atom experiments in optical lattices offer a versatile platform to realize various topological quantum phases. A key challenge in those experiments is to unambiguously probe the topological order. We propose a method to directly measure the characteristic topological invariants (order) based on the time-of-flight imaging of cold atoms. The method is generally applicable to detection of topological band insulators in one, two, or three dimensions characterized by integer topological invariants. Using detection of the Chern number for the 2D anomalous quantum Hall states and the Chern-Simons term for the 3D chiral topological insulators as examples, we show that the proposed detection method is practical, robust to typical experimental imperfections such as limited imaging resolution, inhomogeneous trapping potential, and disorder in the system.

PACS numbers: 03.65.Vf, 67.85.-d, 37.10.Jk

The study of topological phases of matter, such as topological band insulators and superconductors, has attracted a lot of interest in recent years [1–3]. Various topological phases have been found associated with the free-fermion band theory and classified into a periodic table according to the system symmetry and dimensionality [4–6]. The topology of the band structure is characterized by a topological invariant taking only integer values, which gives the most direct and unambiguous signal of the corresponding topological order. To experimentally probe the topological order, it is desirable to have a way to measure the underlying topological invariant. For some phase, the topological invariant may manifest itself through certain quantized transport property or characteristic edge state behavior [7]. For instance, the quantized Hall conductivity is proportional to the underlying topological Chern number that characterizes the integer quantum Hall states [7–9]. For many other topological phases in the periodic table, it is not clear yet how to experimentally extract information of the underlying topological invariants.

Cold atoms in optical lattices provide a powerful experimental platform to simulate various quantum states of matter. In particular, recent experimental advance in engineering of spin-orbit coupling and artificial gauge field for cold atoms [10–15] has pushed this system to the forefront for realization of various topological quantum phases [16–22]. The detection method for cold-atom experiments is usually quite different from those for conventional solid-state materials. A number of intriguing proposals have been made for detection of certain topological order in cold-atom experiments, such as those based on the dynamic response [23–26], the Bragg spectroscopy [27, 28], imaging of the edge states [29], counting peaks in the momentum distribution [30] or detection of the Berry phase or curvature [1, 26, 32–38]. Most of these proposals are targeted to detection of the quantum Hall

phase. Similar to solid-state systems, it is not clear yet how to probe the topological invariants for various other topological phases in the periodic table.

In this Rapid Communication, we propose a general method to directly measure the topological invariants in cold-atom experiments based on the state-of-the-art time-of-flight (TOF) imaging. The TOF imaging, combined with the quench dynamics from the Hamiltonian, has been exploited in recent schemes for detection of the Chern numbers associated with two-band topological models in one or two dimensional optical lattices [26]. Compared with the previous work, our method has the following distinctive features: 1) it is applicable to detection of any topological band insulators with spin degrees of freedom in one, two, or three dimensions that are characterized by integer topological invariants in the periodic table. 2) The method is not limited by the requirement of a two-band structure for the Hamiltonian [1, 26] or occupation of only the lowest band [33]. Instead, it detects the topological invariants associated with each band for any multi-band Hamiltonians. 3) Our proposed detection method is very robust to practical experimental imperfections. As examples, we numerically simulate two experimental detections: one for the Chern number of the 2D anomalous quantum Hall phase and the other for the Chern-Simons term of the 3D chiral topological insulator. Both simulations show that accurate values of the topological invariants can be obtained experimentally under imaging resolution of a few to a dozen pixels along each spatial dimension, even with inhomogeneous traps and random potentials or interactions. The robustness is also found in Ref. [26] for detection of the Chern number in a different 2D model using the tomography method.

The topological band insulators are described by effective free-fermion Hamiltonians, typically with complicated spin-orbit couplings. We consider a real-space Hamiltonian with  $N$  spin (pseudo-spin) degrees of freedom, referred as  $|m\rangle$  with  $m = 1, 2, \dots, N$ . In the momentum  $\mathbf{k}$  space, the Hamiltonian has  $N$  bands and is described by an  $N$ -by- $N$  Hermitian matrix  $H(\mathbf{k})$ . The

\* dldeng@umich.edu

energy spectrum is obtained by solving the Schrödinger equation in the momentum space

$$H(\mathbf{k})|u_b(\mathbf{k})\rangle = E_b(\mathbf{k})|u_b(\mathbf{k})\rangle, \quad (1)$$

where  $b = 1, 2, \dots, N$  is the band index and  $|u_b(\mathbf{k})\rangle$  denotes the corresponding Bloch state with eigen-energy  $E_b(\mathbf{k})$ . For simplicity, we assume the bands are non-degenerate. Expressed in the original spin basis  $|m\rangle$ , the Bloch state has the form

$$|u_b(\mathbf{k})\rangle = \sum_{m=1}^N c_{bm}(\mathbf{k})|m\rangle, \quad (2)$$

where  $c_{bm}(\mathbf{k})$  is the Bloch wavefunction with normalization  $\sum_m |c_{bm}(\mathbf{k})|^2 = 1$ .

An topological invariant can be defined for each band, which usually takes the form of the Chern numbers for even spatial dimensions and the Chern-Simons terms (or the winding numbers in certain cases) for odd spatial dimensions. The Chern numbers (or Chern-Simons terms) can be expressed as momentum-space integrals of the Berry curvature and connection associated with the Bloch state  $|u_b(\mathbf{k})\rangle$ . For instance, in 2D ( $x, y$ -plane), the Chern number  $C_b$  for the band  $b$  is defined by

$$C_b = -\frac{1}{2\pi} \int_{\text{BZ}} dk_x dk_y F_{xy}^{(b)}(\mathbf{k}), \quad (3)$$

where the Berry curvature  $F_{xy}^{(b)}(\mathbf{k}) \equiv \partial_{k_x} A_y^{(b)}(\mathbf{k}) - \partial_{k_y} A_x^{(b)}(\mathbf{k})$  and the Berry connection  $A_\mu^{(b)}(\mathbf{k}) \equiv \langle u_b(\mathbf{k}) | i \partial_{k_\mu} | u_b(\mathbf{k}) \rangle$  ( $\mu = x, y$ ), and the integration is over the whole Brillouin zone (BZ) which forms a compact manifold.

To probe the topological invariant such as the Chern number in Eq. (3), what we need to measure is the Bloch wave function  $c_{bm}(\mathbf{k})$ . The Berry connection and curvature can be obtained as derivatives of  $c_{bm}(\mathbf{k})$  and the Chern number is just a two-fold integration of  $F_{xy}^{(b)}(\mathbf{k})$ . For cold atoms in an optical lattice, we can map out the momentum distribution with the conventional time-of-flight imaging and separate different spin components through a magnetic field gradient [39]. Through the band mapping technique employed in experiments [17], populations in different bands are mapped to atomic densities in different spatial regions, so by this measurement we can get information about  $n_{bm}(\mathbf{k}) = |c_{bm}(\mathbf{k})|^2$  for all occupied bands. To extract the wavefunction  $c_{bm}(\mathbf{k})$ , it is also crucial to measure the phase information. For this purpose, we apply an impulsive pulse right before the flight of atoms to induce a rotation between different spin components [40]. The rotation should keep the atomic momentum unchanged but mix their spins. For instance, a  $\pi/2$ -rotation between spin components  $m$  and  $m'$  induces the transition  $c_{bm}(\mathbf{k}) \rightarrow [c_{bm}(\mathbf{k}) + c_{bm'}(\mathbf{k})]/\sqrt{2}$  and  $c_{bm'}(\mathbf{k}) \rightarrow [-c_{bm}(\mathbf{k}) + c_{bm'}(\mathbf{k})]/\sqrt{2}$ , which can be achieved by applying two co-propagating Raman beams or a radio frequency pulse that couples the spin components  $m, m'$  and preserves the momentum  $\mathbf{k}$ . The

pulse is short so that expansion of the atomic cloud is negligible during the pulse. For Raman pairs, relative phase coherence is kept but absolute phase locking is not necessary. The angular momentum change associated with the spin flip can be transferred from the Raman pair and selection rules have to be followed according to the specific atomic levels used. With this prior  $\pi/2$ -pulse, the time-of-flight (TOF) imaging then measures the densities  $|c_{bm}(\mathbf{k}) \pm c_{bm'}(\mathbf{k})|^2/2$ , whose difference gives the interference terms  $\text{Re}[c_{bm}^*(\mathbf{k})c_{bm'}(\mathbf{k})]$ . By the same method but with a different phase of the  $\pi/2$ -pulse, one can similarly measure the imaginary part  $\text{Im}[c_{bm}^*(\mathbf{k})c_{bm'}(\mathbf{k})]$  between any two spin components  $m$  and  $m'$ . The measurement of the population and interference terms  $c_{bm}^*(\mathbf{k})c_{bm'}(\mathbf{k})$  for all  $m, m'$  fully determines the Bloch wave function  $c_{bm}(\mathbf{k})$  up to arbitrariness of an overall phase  $c_{bm}(\mathbf{k}) \rightarrow c_{bm}(\mathbf{k})e^{i\varphi(\mathbf{k})}$ , where  $\varphi(\mathbf{k})$  in general is  $\mathbf{k}$ -dependent but independent of the spin index.

In experiments, one needs to discretize the TOF image and measure the density distribution at each pixel of the BZ. The wavefunction  $c_{bm}(\mathbf{k})$  is fixed up to an overall phase  $\varphi(\mathbf{k})$  at each pixel with the above method. This arbitrary  $\mathbf{k}$ -dependent phase poses an obstacle to measurement of the topological invariants. To overcome this difficulty, we use a different way to calculate the Berry curvature based on the so-called  $U(1)$ -link defined for each pixel  $\mathbf{k}_J$  of the discrete BZ [41]. The  $U(1)$ -link is defined as  $U_\nu^{(b)}(\mathbf{k}_J) \equiv \langle u_b(\mathbf{k}_J) | u_b(\mathbf{k}_{J+\hat{\nu}}) \rangle / \langle u_b(\mathbf{k}_J) | u_b(\mathbf{k}_{J+\hat{\nu}}) \rangle$ , where  $\hat{\nu} = \hat{x}, \hat{y}, \hat{z}$ , a unit vector in the corresponding direction. A gauge-independent field is obtained from the  $U(1)$ -link as [41]

$$\mathcal{F}_{\mu\nu}^{(b)}(\mathbf{k}_J) \equiv i \ln \frac{U_\mu^{(b)}(\mathbf{k}_J) U_\nu^{(b)}(\mathbf{k}_{J+\hat{\mu}})}{U_\mu^{(b)}(\mathbf{k}_{J+\hat{\nu}}) U_\nu^{(b)}(\mathbf{k}_J)}, \quad (4)$$

where  $\mathcal{F}_{\mu\nu}^{(b)}(\mathbf{k}_J) \in (-\pi, \pi]$  corresponds to a discrete version of the Berry curvature and it reduces to the latter in the large size limit.  $\mathcal{F}_{\mu\nu}^{(b)}(\mathbf{k}_J)$  can be obtained directly from the TOF images associated with the pixel  $\mathbf{k}_J$  of the BZ, independent of the overall phase factor  $\varphi(\mathbf{k})$ . The topological invariant can be calculated from  $\mathcal{F}_{\mu\nu}^{(b)}(\mathbf{k}_J)$  by a direct summation over all the pixels of the BZ (instead of  $\mathbf{k}$  integration in Eq. (3)). This gives a simple and robust way to experimentally extract the topological invariant from the TOF images.

The detection method described above is general and applicable to various topological phases in different spatial dimensions. To show that the method is robust to experimental imperfections, in the following we numerically simulate detection of two kinds of topological invariants: one is the Chern number associated with the 2D quantum anomalous Hall effect and the other is the Chern-Simons term associated with the 3D chiral topological insulator.

*2D quantum anomalous Hall (QAH) effect*— The conventional quantum Hall effect requires application of a strong magnetic field. For the QAH effect, a combination of spontaneous magnetization and spin-orbit coupling gives rise to quantized Hall conductivity in the ab-

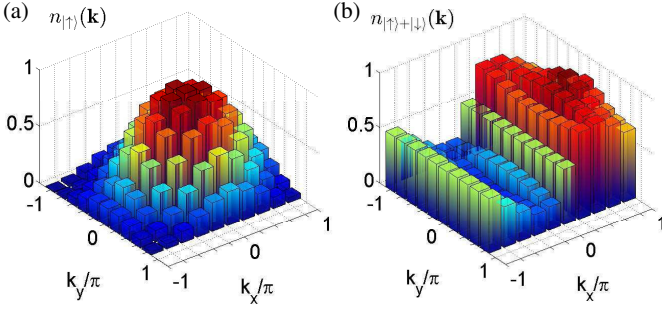


Figure 1. (color online). Density distributions in momentum space for the first band of  $H_{\text{QAH}}$  under two different spin bases with lattice size  $10 \times 10$  and open boundary condition. The total density at each  $\mathbf{k}$  is normalized to unity (e.g.,  $n_{|\uparrow\rangle}(\mathbf{k}) + n_{|\downarrow\rangle}(\mathbf{k}) = 1$ ) corresponding to the unit filling. The parameters are chosen to be  $\lambda_{\text{SO}}^{(x)} = \lambda_{\text{SO}}^{(y)} = h = t$ ,  $\gamma_T = 0.01t$ , and  $\gamma_P = 0.1t$ .

sence of an external magnetic field [42]. In solid-state systems, a recent experiment has observed this peculiar phenomenon in thin films of a magnetically doped topological insulator [43]. A simple square-lattice Hamiltonian which captures the essential physics of the QAH effect has the following form in real space:

$$H_{\text{QAH}} = \lambda_{\text{SO}}^{(x)} \sum_{\mathbf{r}} [(a_{\mathbf{r}\uparrow}^\dagger a_{\mathbf{r}+\hat{x}\downarrow} - a_{\mathbf{r}\uparrow}^\dagger a_{\mathbf{r}-\hat{x}\downarrow}) + \text{H.c.}] \quad (5)$$

$$+ i\lambda_{\text{SO}}^{(y)} \sum_{\mathbf{r}} [(a_{\mathbf{r}\uparrow}^\dagger a_{\mathbf{r}+\hat{y}\downarrow} - a_{\mathbf{r}\uparrow}^\dagger a_{\mathbf{r}-\hat{y}\downarrow}) + \text{H.c.}]$$

$$- t \sum_{\langle \mathbf{r}, \mathbf{s} \rangle} (a_{\mathbf{r}\uparrow}^\dagger a_{\mathbf{s}\uparrow} - a_{\mathbf{r}\downarrow}^\dagger a_{\mathbf{s}\downarrow}) + h \sum_{\mathbf{r}} (a_{\mathbf{r}\uparrow}^\dagger a_{\mathbf{r}\uparrow} - a_{\mathbf{r}\downarrow}^\dagger a_{\mathbf{r}\downarrow}),$$

where  $a_{\mathbf{r}\sigma}^\dagger$  ( $a_{\mathbf{r}\sigma}$ ) is the creation (annihilation) operator of the fermionic atom with pseudospin  $\sigma = (\uparrow, \downarrow)$  at site  $\mathbf{r}$ , and  $\hat{x}, \hat{y}$  are unit lattice vectors along the  $x, y$  directions. The first term in the Hamiltonian describes the spin-orbit coupling. The second and the third terms denote respectively the spin-conserved nearest-neighbor hopping and the Zeeman interaction. It was proposed recently that  $H_{\text{QAH}}$  may be realized with cold fermionic atoms trapped in a blue-detuned optical lattice [44].

In momentum space, this Hamiltonian has two Bloch bands. The topological structure of this model is characterized by the Chern number defined in Eq. (3). Direct calculation shows that  $C_2 = -C_1 = \text{sign}(h)$  when  $0 < |h| < 4t$  and  $C_2 = -C_1 = 0$  otherwise. Experimentally, one can measure  $\mathcal{F}_{\mu\nu}^{(b)}(\mathbf{k}_{\mathbf{J}})$  by our proposed method to extract the Chern number through  $C_b \approx -\sum_{\mathbf{J}} \mathcal{F}_{xy}^{(b)}(\mathbf{k}_{\mathbf{J}})/(2\pi)$ , where the band index  $b = 1, 2$ .

To simulate experiments, we consider a finite-size lattice with open boundary condition. In addition, we add a global harmonic trap of the form  $V_T = m_a \omega^2 r^2/2$  for atoms of mass  $m_a$  as in real experiments and use  $\gamma_T = m_a \omega^2 a^2/2t$  to parameterize the relative strength of the trap, where  $a$  denotes the lattice constant. To account for possible experimental noise, we add a random

Table I. Simulated detection results of the topological invariants for different lattice sizes under various conditions (Periodic boundary condition, Open boundary condition, with Trap, with both Trap and Perturbation Hamiltonians). For the QAH, the invariant is the Chern number for the first band ( $C_1$ ), whereas for the CTI, it is the Chern-Simons term for the middle flat band ( $CS_2/\pi$ ). Results for both the nontrivial phase ( $h/t = 1$  for the QAH and  $h/t = 2$  for the CTI) and the trivial phase ( $h/t = 5$  for the QAH and  $h/t = 4$  for the CTI) are presented. The parameters are the same as in Fig. 1 and Fig. 2.

	$h/t$	Size	Periodic	Open	Trap	Pert.+Trap
QAH	1	$4^2$	-1	-1	-1	-1
	1	$10^2$	-1	-1	-1	-1
	5	$10^2$	0	0	0	0
CTI	2	$10^3$	1.041	1.056	1.055	1.080
	2	$12^3$	1.031	1.009	0.981	1.014
	4	$10^3$	0	$-2 * 10^{-4}$	$1.1 * 10^{-3}$	$1.2 * 10^{-3}$

perturbation Hamiltonian of the following general form

$$H_P = \gamma_P t \sum_{\langle \mathbf{r}, \mathbf{s} \rangle, \alpha, \beta} a_{\mathbf{r}, \alpha}^\dagger \mathcal{P}_{\mathbf{r}\alpha, \mathbf{s}\beta} a_{\mathbf{s}, \beta}, \quad (6)$$

where  $\gamma_P$  is a dimensionless parameter characterizing the strength of random perturbation,  $\langle \mathbf{r}, \mathbf{s} \rangle$  denotes the neighboring sites, and  $\mathcal{P}$  is a random Hermitian matrix with its largest eigenvalue normalized to unity. We numerically diagonalize the real-space Hamiltonian on a finite lattice with different number of sites and calculate the corresponding momentum density distributions [45]. An example, in Fig. 1, we show the reconstructed density distribution in two complementary bases ( $\{|\uparrow\rangle, |\downarrow\rangle\}$ ,  $\{|\uparrow\rangle \pm |\downarrow\rangle\}$ ) under open boundary condition with a harmonic trap and random perturbations (more detailed calculation results are shown in the supplement [45]). The Chern numbers for each case are calculated and listed in Table II under choices of different parameters and system sizes. The extracted Chern numbers exactly equal the corresponding theoretical values, even under a small system size and significant disorder potentials. This is so as Chern numbers characterize the topological property, which does not change under perturbations. Furthermore, our detection method through measurement of  $\mathcal{F}_{\mu\nu}^{(b)}(\mathbf{k}_{\mathbf{J}})$  guarantees an integer value for the extracted Chern number [41], so it automatically corrects small errors due to experimental imperfections. Ref. [26] also points out the robustness of Fukui *et al.*'s method [41] in computing the Chern number.

*3D chiral topological insulator*—Chiral topological insulators (CTIs) are protected by the chiral symmetry (also known as the sub-lattice symmetry) and belong to the AIII class in the periodic table for topological phases [4–6]. A simple Hamiltonian that supports 3D CTIs has

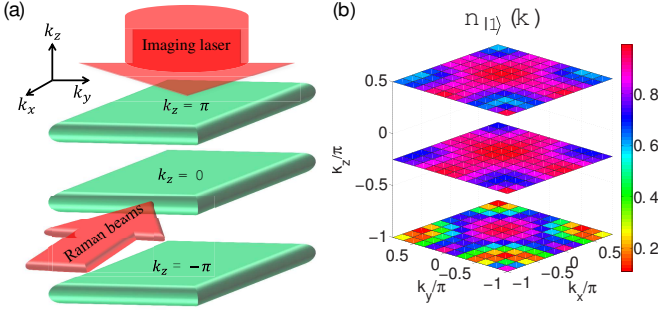


Figure 2. (color online). (a) An illustration to show reconstruction of the 3D atomic momentum distribution by the TOF imaging. (b) Momentum distribution in one particular spin basis (other results are shown in the supplement [45]) for the middle flat band of  $H_{CTI}$  with open boundary condition under lattice size  $12 \times 12 \times 12$ . Layers corresponding to  $k_z = -\pi, -\pi/4, \pi/2$  are displayed. The parameters are  $h = 2t$ ,  $\gamma_T = 0.001t$ ,  $\gamma_P = 0.1t$ .

the form [3]:

$$H_{CTI} = \frac{t}{2} \sum_{\mathbf{r}} \sum_{j=1}^3 [\psi_{\mathbf{r}}^\dagger (iG_{3+j} - G_7) \psi_{\mathbf{r}+\mathbf{e}_j} + \text{H.c.}] + h \sum_{\mathbf{r}} \psi_{\mathbf{r}}^\dagger G_7 \psi_{\mathbf{r}}, \quad (7)$$

where the operator  $\psi_{\mathbf{r}}^\dagger = (a_{\mathbf{r},1}^\dagger, a_{\mathbf{r},2}^\dagger, a_{\mathbf{r},3}^\dagger)$  with  $a_{\mathbf{r},\alpha}^\dagger$  ( $\alpha = 1, 2, 3$ ) creating a fermion at site  $\mathbf{r}$  with spin state  $\alpha$ ,  $\mathbf{e}_1, \mathbf{e}_2, \mathbf{e}_3$  are unit vectors along the  $x, y, z$  directions, and  $G_\nu$  ( $\nu = 4, 5, 6, 7$ ) denotes the  $\nu$ th Gell-Mann matrix [45]. In the momentum space, this model Hamiltonian has three gapped bands, with a zero-energy flat band in the middle protected by the chiral symmetry. An experimental scheme has been proposed to realize this model Hamiltonian with cold fermionic atoms in an optical lattice [2]. The topological property of this Hamiltonian can be described by the Chern-Simons term. For the  $b$ -th ( $b = 1, 2, 3$ ) Bloch band, the Chern-Simons term  $CS_b$  takes the form

$$CS_b = -\frac{1}{4\pi} \int_{\text{BZ}} d\mathbf{k} \epsilon^{\mu\nu\tau} A_\mu^{(b)}(\mathbf{k}) \partial_{k_\nu} A_\tau^{(b)}(\mathbf{k}), \quad (8)$$

where  $A_\mu^{(b)}(\mathbf{k}) = \langle u_b(\mathbf{k}) | \partial_{k_\mu} | u_b(\mathbf{k}) \rangle$  ( $\mu = x, y, z$ ). Explicit calculations show that  $CS_3 = CS_1 = CS_2/4 = \pi\Gamma(h)/4$  with  $\Gamma(h) = -2$  for  $|h| < t$ ,  $\Gamma(h) = 1$  for  $t < |h| < 3t$ , and  $\Gamma(h) = 0$  otherwise.

As an example application of our general detection method, here we show how to measure the topological invariant  $CS_b$  through the TOF imaging. As shown in Fig. 2(a), we first use the TOF imaging to reconstruct the 3D atomic momentum distribution. After expansion of the atomic cloud, we apply a pair of co-propagating Raman beams focused in the  $z$ -axis to transfer a layer of atoms with a fixed  $z$ -coordinate  $z_i$  to another hyperfine or Zeeman level denoted as  $|r\rangle$ . We apply the imaging laser to couple the atoms only on the  $|r\rangle$  level, so the imaging reads out the 2D momentum distribution  $n(k_x, k_y, k_{z_i})$  with a fixed  $k_{z_i} \propto z_i$ . We repeat this measurement by scanning the coordinate  $z_i$  so that each image gives a 2D distribution  $n(k_x, k_y, k_{z_i})$  with a different  $k_{z_i}$ . By this method, we reconstruct the 3D momentum distribution  $n(k_x, k_y, k_z)$ , where  $l$  images give  $l$  pixels of  $k_z$ .

To extract the Chern-Simons term  $CS_b$ , we measure the 3D momentum distribution  $n_{bm}(k_x, k_y, k_z)$  in different spin bases to obtain the Bloch wave function  $c_{bm}(\mathbf{k})$ . We then use the measured  $c_{bm}(\mathbf{k})$  to calculate the gauge independent field  $\mathcal{F}_{\mu\nu}^{(b)}(\mathbf{k}_J)$  defined in Eq. (4). By solving a discrete version of the equation  $\nabla \times \mathbf{A} = \mathbf{F}$  in the momentum space with the Coulomb gauge  $\nabla \cdot \mathbf{A} = 0$ , we obtain the Berry connection  $A_\mu^{(b)}(\mathbf{k}_J)$  from  $\mathcal{F}_{\mu\nu}^{(b)}(\mathbf{k}_J)$ . With  $A_\mu^{(b)}$ , we extract the Chern-Simons term  $CS_b$  using Eq. (8).

The Chern-Simons terms extracted from our numerically simulated experiments are shown in Table II under various conditions. Different from the Chern number case, extraction of the Chern-Simons term using Eq. (8) does not guarantee the result to be an integer, so the calculated values are subject to influence of numerical inaccuracies and experimental noise. Nevertheless, from the results listed in Table II, we see that the extracted values quickly approach the corresponding theoretical limits when we take a dozen of pixels along each spatial dimension in the time-of-flight imaging and the detection method remains robust to experimental imperfections (traps and random perturbation Hamiltonians change the result by less than 3%).

In summary, we have proposed a general method to experimentally measure the topological invariants for ultracold atoms. The method is shown to be robust to various experimental imperfections through numerically simulated experiments.

We thank S.-L. Zhu for discussions. This work was supported by the NBRPC (973 Program) 2011CBA00300 (2011CBA00302), the IARPA MUSIQ program, the ARO and the AFOSR MURI program.

[1] M. Z. Hasan and C. L. Kane, Rev. Mod. Phys. **82**, 3045 (2010).  
 [2] X.-L. Qi and S.-C. Zhang, Rev. Mod. Phys. **83**, 1057 (2011).  
 [3] J. E. Moore, Nature **464**, 194 (2010).

[4] A. P. Schnyder, S. Ryu, A. Furusaki, and A. W. Ludwig, Phys. Rev. B **78**, 195125 (2008).  
 [5] A. Kitaev, in *AIP Conference Proceedings*, Vol. 1134 (2009) p. 22.  
 [6] S. Ryu, A. P. Schnyder, A. Furusaki, and A. W. Ludwig,



- New J. Phys. **12**, 065010 (2010).
- [7] D. Thouless, M. Kohmoto, M. Nightingale, and M. Den Nijs, Phys. Rev. Lett. **49**, 405 (1982).
  - [8] K. von Klitzing, Rev. Mod. Phys. **58** (1986).
  - [9] S. D. Sarma and A. Pinczuk, *Perspectives in quantum Hall effects* (John Wiley & Sons, 2008).
  - [10] Y.-J. Lin, R. L. Compton, K. Jimenez-Garcia, J. V. Porto, and I. B. Spielman, Nature **462**, 628 (2009).
  - [11] X.-J. Liu, M. F. Borunda, X. Liu, and J. Sinova, Phys. Rev. Lett. **102**, 046402 (2009).
  - [12] P. Wang, Z.-Q. Yu, Z. Fu, J. Miao, L. Huang, S. Chai, H. Zhai, and J. Zhang, Phys. Rev. Lett. **109**, 095301 (2012).
  - [13] L. W. Cheuk, A. T. Sommer, Z. Hadzibabic, T. Yefsah, W. S. Bakr, and M. W. Zwierlein, Phys. Rev. Lett. **109**, 095302 (2012).
  - [14] J. Dalibard, F. Gerbier, G. Juzeliūnas, and P. Öhberg, Rev. Mod. Phys. **83**, 1523 (2011).
  - [15] V. Galitski and I. B. Spielman, Nature **494**, 49 (2013).
  - [16] M. Lewenstein, A. Sanpera, V. Ahufinger, B. Damski, A. Sen, and U. Sen, Adv. Phys. **56**, 243 (2007).
  - [17] I. Bloch, J. Dalibard, and S. Nascimbène, Nat. Phys. **8**, 267 (2012).
  - [18] S.-L. Zhu, H. Fu, C.-J. Wu, S.-C. Zhang, and L.-M. Duan, Phys. Rev. Lett. **97**, 240401 (2006).
  - [19] S.-L. Zhu, L.-B. Shao, Z. Wang, and L.-M. Duan, Phys. Rev. Lett. **106**, 100404 (2011).
  - [20] B. Béri and N. Cooper, Phys. Rev. Lett. **107**, 145301 (2011).
  - [21] M. Aidelsburger, M. Atala, M. Lohse, J. Barreiro, B. Paredes, and I. Bloch, Phys. Rev. Lett. **111**, 185301 (2013).
  - [22] H. Miyake, G. A. Siviloglou, C. J. Kennedy, W. C. Burton, and W. Ketterle, Phys. Rev. Lett. **111**, 185302 (2013).
  - [23] L. Shao, S.-L. Zhu, L. Sheng, D. Xing, and Z. Wang, Phys. Rev. Lett. **101**, 246810 (2008).
  - [24] A. Dauphin and N. Goldman, Phys. Rev. Lett. **111**, 135302 (2013).
  - [25] L. Wang, A. A. Soluyanov, and M. Troyer, Phys. Rev. Lett. **110**, 166802 (2013).
  - [26] P. Hauke, M. Lewenstein, and A. Eckardt, Phys. Rev. Lett. **113**, 045303 (2014).
  - [27] X.-J. Liu, X. Liu, C. Wu, and J. Sinova, Phys. Rev. A **81**, 033622 (2010).
  - [28] N. Goldman, J. Beugnon, and F. Gerbier, Phys. Rev. Lett. **108**, 255303 (2012).
  - [29] N. Goldman, J. Dalibard, A. Dauphin, F. Gerbier, M. Lewenstein, P. Zoller, and I. B. Spielman, Proc. Natl. Acad. Sci. **110**, 6736 (2013).
  - [30] E. Zhao, N. Bray-Ali, C. J. Williams, I. B. Spielman, and I. I. Satija, Phys. Rev. A **84**, 063629 (2011).
  - [31] E. Alba, X. Fernandez-Gonzalvo, J. Mur-Petit, J. Pachos, J. J. García-Ripoll, *et al.*, Phys. Rev. Lett. **107**, 235301 (2011).
  - [32] H. Price and N. Cooper, Phys. Rev. A **85**, 033620 (2012).
  - [33] X.-J. Liu, K. Law, T. Ng, and P. A. Lee, Phys. Rev. Lett. **111**, 120402 (2013).
  - [34] D. A. Abanin, T. Kitagawa, I. Bloch, and E. Demler, Phys. Rev. Lett. **110**, 165304 (2013).
  - [35] M. Atala, M. Aidelsburger, J. T. Barreiro, D. Abanin, T. Kitagawa, E. Demler, and I. Bloch, Nat. Phys. **9**, 795 (2013).
  - [36] N. Goldman, E. Anisimovas, F. Gerbier, P. Öhberg, I. B. Spielman, and G. Juzeliūnas, New J. Phys. **15**, 013025 (2013).
  - [37] J. K. Pachos, E. Alba, V. Lahtinen, and J. J. Garcia-Ripoll, Phys. Rev. A **88**, 013622 (2013).
  - [38] J. de Lisle, S. De, E. Alba, A. Bullivant, J. J. Garcia-Ripoll, V. Lahtinen, and J. K. Pachos, arXiv:1402.3222v2.
  - [39] W. Ketterle and M. Zwierlein, Riv. Nuovo Cimento **31**, 247 (2008).
  - [40] L.-M. Duan, Phys. Rev. Lett. **96**, 103201 (2006).
  - [41] T. Fukui, Y. Hatsugai, and H. Suzuki, J. Phys. Soc. Jpn. **74**, 1674 (2005).
  - [42] F. Haldane, Phys. Rev. Lett. **61**, 2015 (1988).
  - [43] C.-Z. Chang, J. Zhang, X. Feng, J. Shen, Z. Zhang, M. Guo, K. Li, Y. Ou, P. Wei, L.-L. Wang, *et al.*, Science **340**, 167 (2013).
  - [44] X.-J. Liu, K. T. Law, and T. K. Ng, Phys. Rev. Lett. **112**, 086401 (2014).
  - [45] See Supplemental Material at [URL will be inserted by publisher] for more details on the calculations of the momentum density distributions and more plots of the numerical simulations..
  - [3] T. Neupert, L. Santos, S. Ryu, C. Chamon, and C. Mudry, Phys. Rev. B **86**, 035125 (2012).
  - [2] S.-T. Wang, D.-L. Deng, and L.-M. Duan, Phys. Rev. Lett. **113**, 033002 (2014).

## SUPPLEMENTARY MATERIAL: DIRECT PROBE OF TOPOLOGICAL ORDER FOR COLD ATOMS

This supplementary material gives more details on numerical simulation of the experimental detection and extraction of the topological invariants. In section I, we show how to numerically calculate the atomic momentum distribution by solving the real-space Hamiltonians under open boundary condition. In section II, we provide details on how the random perturbation and harmonic trapping potential are incorporated into the simulation. In Sec. III, we include more detailed results from the numerical simulations as well as an explicit definition of the Gell-Mann matrices used in the main text.

### Appendix A: Numerical simulation of the atomic momentum distribution

In this section, we provide more details on how to numerically simulate the atomic momentum distribution by solving real-space Hamiltonians. Consider a generic quadratic Hamiltonian in real space that describe free fermions:

$$H = \sum_{\mathbf{r}, \mathbf{s}, \alpha, \beta} a_{\mathbf{r}, \alpha}^\dagger \mathcal{H}_{\mathbf{r}\alpha, \mathbf{s}\beta} a_{\mathbf{s}, \beta}, \quad (\text{A1})$$

where  $a_{\mathbf{r}, \alpha}^\dagger (a_{\mathbf{s}, \beta})$  creates (annihilates) a particle at lattice site  $\mathbf{r}(\mathbf{s})$  with pseudospin  $\alpha(\beta)$ . One can solve the Schrödinger equation  $\mathcal{H}\Phi_i = \epsilon_i\Phi_i$  to obtain the single-particle energy spectrum. In the matrix form, one can diagonalize  $\mathcal{H}$  by a unitary transformation  $U$ :  $\mathcal{H} = U^\dagger \mathcal{E} U$  to find the single-particle eigenmodes  $b_{\mathbf{r}, \alpha} = \sum_{\mathbf{s}, \beta} U_{\mathbf{r}\alpha, \mathbf{s}\beta} a_{\mathbf{s}, \beta}$ . Here  $\mathcal{E} = \text{diag}(\epsilon_1, \epsilon_2, \dots)$  is a diagonal matrix. For a free-fermion system described by Eq. (A1), the total particle number  $\mathcal{N} = \sum_{\mathbf{r}, \alpha} a_{\mathbf{r}, \alpha}^\dagger a_{\mathbf{r}, \alpha}$  is a conserved quantity  $[H, \mathcal{N}] = 0$ . These  $\mathcal{N}$  particles will occupy the first  $\mathcal{N}$  eigenmodes with lowest eigenenergies. Consequently, the ground state of the system reads

$$|G\rangle = \prod_{i=1}^{\mathcal{N}} b_i^\dagger |0\rangle, \quad (\text{A2})$$

where we suppress  $\mathbf{r}$  and  $\alpha$  into a single index  $i$  for the occupied eigenmodes, and  $|0\rangle$  is the vacuum state without any particles. The density distribution in momentum space can then be obtained as

$$n_\alpha(\mathbf{k}) = \langle G | a_\alpha^\dagger(\mathbf{k}) a_\alpha(\mathbf{k}) | G \rangle. \quad (\text{A3})$$

where  $a_\alpha(\mathbf{k})$  relates to  $a_{\mathbf{r}, \alpha}$  by a Fourier transform,

$$\begin{aligned} n_\alpha(\mathbf{k}) &= \langle G | \frac{1}{\sqrt{\mathcal{L}}} \sum_{\mathbf{r}} e^{i\mathbf{k} \cdot \mathbf{r}} a_{\mathbf{r}, \alpha}^\dagger \frac{1}{\sqrt{\mathcal{L}}} \sum_{\mathbf{r}'} e^{-i\mathbf{k} \cdot \mathbf{r}'} a_{\mathbf{r}', \alpha} | G \rangle \\ &= \frac{1}{\mathcal{L}} \sum_{\mathbf{r}, \mathbf{r}'} \langle G | a_{\mathbf{r}, \alpha}^\dagger a_{\mathbf{r}', \alpha} | G \rangle e^{i\mathbf{k} \cdot (\mathbf{r} - \mathbf{r}')}, \end{aligned} \quad (\text{A4})$$

where  $\mathcal{L}$  denotes the number of lattice sites. As  $a_{\mathbf{r}, \alpha} = \sum_{\mathbf{s}, \beta} (U^\dagger)_{\mathbf{r}\alpha, \mathbf{s}\beta} b_{\mathbf{s}, \beta}$ , the quantity  $\langle G | a_{\mathbf{r}, \alpha}^\dagger a_{\mathbf{r}', \alpha} | G \rangle$  can be further simplified:

$$\begin{aligned} \langle G | a_{\mathbf{r}, \alpha}^\dagger a_{\mathbf{r}', \alpha} | G \rangle &= \langle G | \sum_{\mathbf{s}, \beta} (U^\dagger)_{\mathbf{r}\alpha, \mathbf{s}\beta}^* b_{\mathbf{s}, \beta}^\dagger \sum_{\mathbf{s}', \beta'} (U^\dagger)_{\mathbf{r}'\alpha, \mathbf{s}'\beta'} b_{\mathbf{s}', \beta'} | G \rangle \\ &= \sum_{\mathbf{s}, \beta, \mathbf{s}', \beta'} \langle G | b_{\mathbf{s}, \beta}^\dagger b_{\mathbf{s}', \beta'} | G \rangle (U^\dagger)_{\mathbf{r}\alpha, \mathbf{s}\beta}^* (U^\dagger)_{\mathbf{r}'\alpha, \mathbf{s}'\beta'} \\ &= \sum_i^{\mathcal{N}} (U^\dagger)_{\mathbf{r}\alpha, i}^* (U^\dagger)_{\mathbf{r}'\alpha, i}. \end{aligned} \quad (\text{A5})$$

In the last step of Eq. (A5), we have used the following equation

$$\langle G | b_{\mathbf{s}, \beta}^\dagger b_{\mathbf{s}', \beta'} | G \rangle = \begin{cases} 1 & \text{if } \mathbf{s} = \mathbf{s}', \beta = \beta' \text{ and the eigen-mode } b_{\mathbf{s}, \beta} \text{ is occupied} \\ 0 & \text{otherwise.} \end{cases}$$

Combining Eq. (A5) and Eq. (A4), we can obtain the momentum density distribution for each pseudospin component from a generic quadratic real-space Hamiltonian with a specific filling fraction (the filling fraction is defined as the total particle number divided by the lattice site number:  $f = \mathcal{N}/\mathcal{L}$ ). Analogously, one can rotate the pseudospin and use the same method to compute the momentum density distribution in other spin bases  $n_{a|\alpha\rangle+b|\beta\rangle}(\mathbf{k})$ .

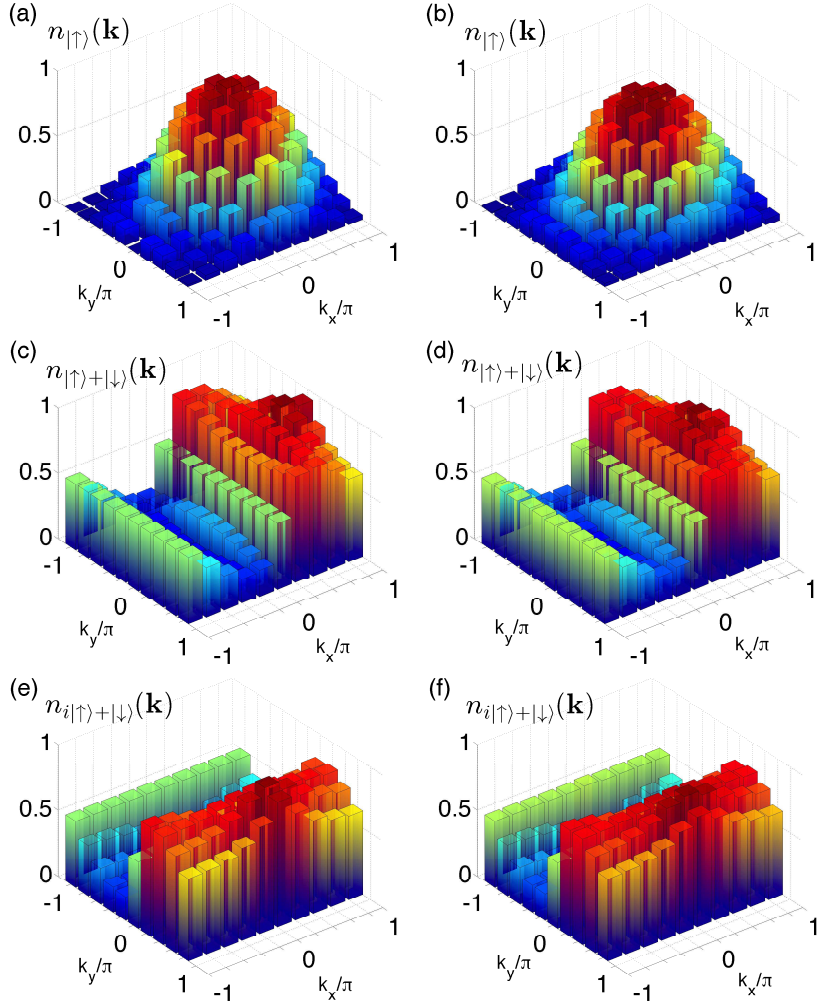


Figure 3. (color online). Density distributions in momentum space for the first band with lattice size  $10 \times 10$ . (a), (c) and (e) correspond to the periodic boundary condition without perturbation and trapping potential; (b), (d), and (f) correspond to open boundary conditions with random perturbations and harmonic trapping (subfigures (b) and (d) are repeated from the main text for clarity and completeness). The parameters used in the calculations are chosen to be  $\lambda_{\text{SO}}^{(x)} = \lambda_{\text{SO}}^{(y)} = t$ ,  $\hbar = t$ ,  $\gamma_{\text{T}} = 0.1t$ , and  $\gamma_{\text{P}} = 0.01t$ . From these distributions, we find the Chern number  $C_1 = -1$  using the formula in the main text.

### Appendix B: Random perturbation and harmonic trapping potential

As discussed in the main text, a typical optical lattice experiment includes a weak harmonic trapping potential,

$$V_{\text{T}} = \frac{1}{2} m_a \omega^2 \sum_{\mathbf{r}, \alpha} d_{\mathbf{r}}^2 a_{\mathbf{r}, \alpha}^\dagger a_{\mathbf{r}, \alpha}, \quad (\text{B1})$$

where  $d_{\mathbf{r}}$  is the distance from the center of the trap to the lattice site  $\mathbf{r}$ ,  $m_a$  is the atomic mass, and  $\omega$  is the trap frequency. In our numerical simulation, we use  $\gamma_{\text{T}} = m_a \omega^2 a^2 / (2t)$  to parametrize the influence of this trapping potential. Here  $a$  is the lattice constant and  $t$  is the hopping rate. For a typical experiment,  $t/\hbar \sim 1\text{kHz}$ ,  $a \sim 400\text{ nm}$ , and  $\gamma_{\text{T}}$  ranges from  $10^{-3}$  ( $^6\text{Li}$  with  $\omega/2\pi = 60\text{ Hz}$ ) to  $2 \times 10^{-2}$  ( $^{40}\text{K}$  with  $\omega/2\pi = 100\text{ Hz}$ ) [1]. To account for other possible experimental noise, we also add a random perturbation term

$$H_{\text{P}} = \gamma_{\text{P}} t \sum_{\mathbf{r}, \mathbf{s}, \alpha, \beta} a_{\mathbf{r}, \alpha}^\dagger \mathcal{P}_{\mathbf{r}\alpha, \mathbf{s}\beta} a_{\mathbf{s}, \beta}, \quad (\text{B2})$$

where  $\mathcal{P}$  is a random Hermitian matrix with its largest eigenvalue normalized to the unity.

In the numerical simulation, we add both  $V_{\text{T}}$  and  $H_{\text{P}}$  into the original Hamiltonians and calculate the momentum density distributions using the method described in Sec. I. Although only partial results are included in Fig. 1, Fig. 2

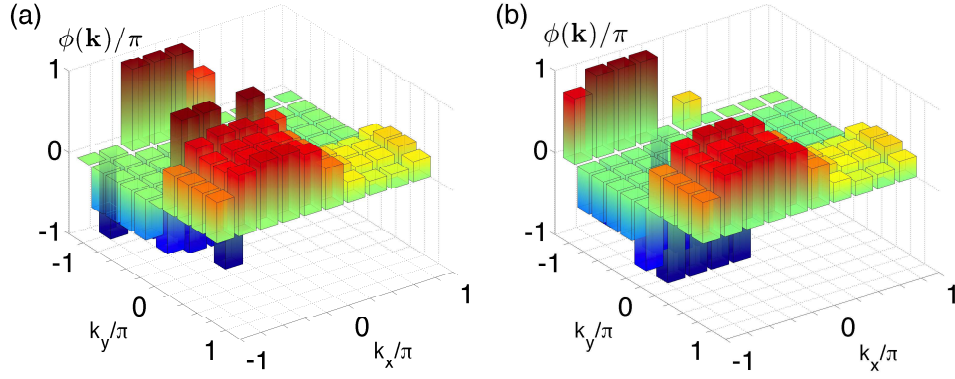


Figure 4. (color online). Relative phase factors in momentum space for the first band of the Hamiltonian  $H_{\text{QAH}}$  with lattice size  $10 \times 10$ . (a) Periodic boundary condition without perturbations and the trapping potential. (b) Open boundary conditions with random perturbations and a harmonic trap. The parameters are chosen to be the same as in Fig. 1 of the main text.

and Table I of the main text, we have done substantial calculations with a number of different choices of parameters  $(\gamma_T, \gamma_P)$  for both the 2D quantum anomalous Hall effect (QAH) and 3D chiral topological insulators (CTIs). Our results consistently show that topological invariants extracted from the time-of-flight (TOF) measurements are very robust to the trapping potential and random perturbations.

### Appendix C: More results from numerical simulation

In this section, we provide more detailed numerical results from numerical simulation of both the 2D QAH and 3D CTI cases.

*2D QAH effect*— In Fig. 1 of the main text, we have plotted two momentum density distributions of the first band. Here, we present more plots of the density distributions in Fig. 3, considering both periodic and open boundary conditions. As discussed in the main text, Fig. 3 (b), (d) and (f) simulate the data obtained from the TOF measurements. To extract the Chern number, an intermediate step is to calculate the relative phase between the spin up and down components of the Bloch wavefunction from those density distributions. A little algebra leads to the following equations:

$$2n_{|\uparrow\rangle+|\downarrow\rangle}(\mathbf{k}) = 1 + 2\sqrt{n_{\uparrow}(\mathbf{k}) \times (1 - n_{\uparrow}(\mathbf{k}))} \cos(\phi(\mathbf{k})) \quad (\text{C1})$$

$$2n_{i|\uparrow\rangle+|\downarrow\rangle}(\mathbf{k}) = 1 + 2\sqrt{n_{\uparrow}(\mathbf{k}) \times (1 - n_{\uparrow}(\mathbf{k}))} \sin(\phi(\mathbf{k})), \quad (\text{C2})$$

where  $\phi(\mathbf{k})$  is defined as the relative phase in the lower band Bloch wavefunction between the spin up and spin down components, i.e.  $|u_1(\mathbf{k})\rangle = |c_{\uparrow}(\mathbf{k})||\uparrow\rangle + |c_{\downarrow}(\mathbf{k})|e^{i\phi(\mathbf{k})}|\downarrow\rangle$ . Plugging the density distributions observed from the TOF measurements into the above equations, one obtains the relative phase. We performed the calculations for both periodic and open boundary conditions and the corresponding relative phases are shown in Fig. 4. With the relative phases and the density distributions, the Bloch wavefunction for the first band is determined up to a momentum-dependent overall phase. Using the method introduced in the main text, we are able to extract the desired Chern number  $C_1 = -1$ .

*3D CTI*— Let us first write down explicitly the four Gell-Mann matrices used in the Hamiltonian  $H_{\text{CTI}}$  in the main text:

$$G_4 = \begin{pmatrix} 0 & 0 & 1 \\ 0 & 0 & 0 \\ 1 & 0 & 0 \end{pmatrix}, \quad G_5 = \begin{pmatrix} 0 & 0 & -i \\ 0 & 0 & 0 \\ i & 0 & 0 \end{pmatrix}, \quad G_6 = \begin{pmatrix} 0 & 0 & 0 \\ 0 & 0 & 1 \\ 0 & 1 & 0 \end{pmatrix}, \quad G_7 = \begin{pmatrix} 0 & 0 & 0 \\ 0 & 0 & -i \\ 0 & i & 0 \end{pmatrix}.$$

A Fourier transform brings  $H_{\text{CTI}}$  to the momentum space [2, 3]:

$$H_{\text{CTI}} = \sum_{\mathbf{k}} \psi_{\mathbf{k}}^{\dagger} \mathcal{H}_{\text{CTI}}(\mathbf{k}) \psi_{\mathbf{k}},$$



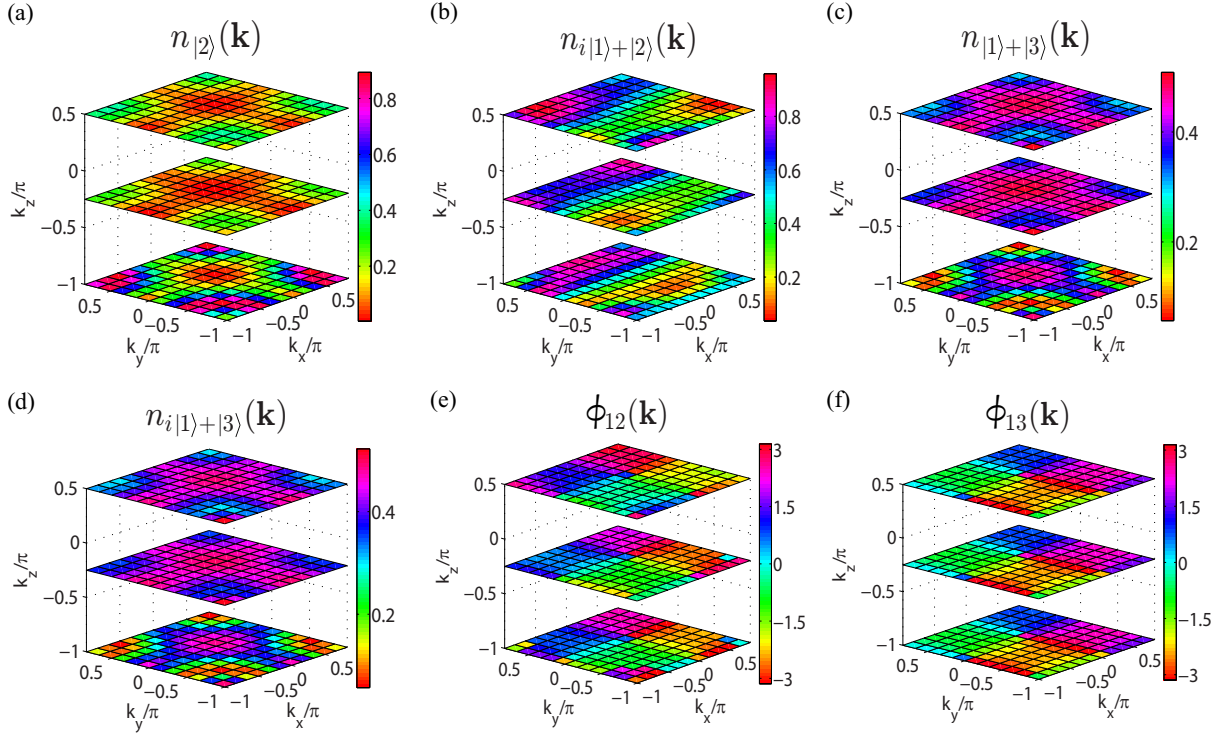


Figure 5. (color online). Momentum density distributions and relative phase factors for the middle flat band with open boundary conditions for  $H_{\text{CTI}}$  including a harmonic trap and some random perturbations. The lattice size is  $12 \times 12 \times 12$ . Layers corresponding to  $k_z = -\pi, -\pi/4, \pi/2$  are displayed.  $\phi_{12}(\mathbf{k})$  ( $\phi_{13}(\mathbf{k})$ ) is the phase factor between spin 1 and 2 (spin 1 and 3) in the Bloch wavefunction. The parameters are chosen to be the same as in Fig. 2 of the main text.

Table II. The Chern-Simons terms of the first and third bands for the Hamiltonian  $H_{\text{CTI}}$ . The parameters are chosen to be the same as in Fig. 2b of the main text.

	Size	$h/t$	Periodic	Open	Trap	Pert.+Trap
CTI ( $CS_1/\pi$ )	$10^3$	2	0.246	0.228	0.231	0.231
	$12^3$	2	0.248	0.228	0.235	0.235
	$10^3$	4	$5.8 \times 10^{-5}$	$8.6 \times 10^{-5}$	$1.5 \times 10^{-4}$	$1.4 \times 10^{-4}$
CTI ( $CS_3/\pi$ )	$10^3$	2	0.246	0.226	0.227	0.227
	$12^3$	2	0.248	0.229	0.230	0.231
	$10^3$	4	$5.8 \times 10^{-5}$	$5.0 \times 10^{-5}$	$1.7 \times 10^{-4}$	$1.8 \times 10^{-4}$

where  $\psi_{\mathbf{k}}^\dagger = (a_{\mathbf{k},1}^\dagger, a_{\mathbf{k},2}^\dagger, a_{\mathbf{k},3}^\dagger)$  and  $\mathcal{H}_{\text{CTI}}(\mathbf{k}) = \sum_{j=1}^4 G_{3+j} q_j(\mathbf{k})$  with  $[q_1(\mathbf{k}), q_2(\mathbf{k}), q_3(\mathbf{k}), q_4(\mathbf{k})] = [\sin k_x, \sin k_y, \sin k_z, m - \cos k_x - \cos k_y - \cos k_z]$ . One can easily check that this Hamiltonian indeed has a chiral symmetry represented by  $S\mathcal{H}_{\text{CTI}}(\mathbf{k})S^{-1} = -\mathcal{H}_{\text{CTI}}(\mathbf{k})$ , where  $S \equiv \text{diag}(1, 1, -1)$  is a unitary matrix. This chiral symmetry leads to an exact zero-energy flat band as discussed in Ref. [2, 3].

In the main text, we plotted some of the momentum density distributions of the middle flat band in Fig. 2(b). Here we include more results of the density distributions and the relative phases in Fig. 5. Analogous to the case of QAH effect, the momentum density distributions can be directly observed from the layered TOF measurements and the relative phases can be calculated from the observed density distributions. After all density distributions are observed in an actual experiment, the Chern-Simons term characterizing the topological structure of the Bloch band can be readily extracted with the method described in the main text.

Besides the Chern-Simons term for the middle flat band shown in Table I of the main text, we have also calculated it for both the first (lowest) and third (highest) bands. Our results are recorded in Table I here. From this table, the extracted Chern-Simons terms converge to the expected theoretical value  $CS_1/\pi = CS_3/\pi = 1/4$  as we increase the lattice size.

- 
- [1] E. Alba, X. Fernandez-Gonzalvo, J. Mur-Petit, J. Pachos, J. J. García-Ripoll, et al., Phys. Rev. Lett. **107**, 235301 (2011).
  - [2] S.-T. Wang, D.-L. Deng, and L.-M. Duan, Phys. Rev. Lett. **113**, 033002 (2014).
  - [3] T. Neupert, L. Santos, S. Ryu, C. Chamon, and C. Mudry, Phys. Rev. B **86**, 035125 (2012).